Research on Engineering Structures & Materials
www.jresm.org
Research Group

Research Article

Bond Behavior between ETS-GFRP strengthening bars and concrete at elevated temperatures: A preliminary analytical and numerical study

Linh Van Hong Bui [1,2,a], Chi Hieu Ma [*,1,2,b]

[1]*Faculty of Civil Engineering, Ho Chi Minh City University of Technology (HCMUT), 268 Ly Thuong Kiet Street, Dien Hong Ward, Ho Chi Minh City, Vietnam*
[2]*Vietnam National University Ho Chi Minh City, Linh Xuan Ward, Ho Chi Minh City, Vietnam*

Article Info

Article History:

Received 15 Jan 2026
Accepted 04 Apr 2026

Keywords:

Bond behavior;
Elevated temperature;
Embedded through-section;
Fiber-reinforced polymer;
Reinforced concrete;
Strengthening

Abstract

The bond behavior of an embedded through-section-glass fiber-reinforced polymer (ETS-GFRP) bar–concrete interface at elevated temperatures is investigated. An analytical bond–slip model is first developed to include both mechanical and thermal variables. By using the finite element method (FEM), the ETS-GFRP bar–concrete interface is simulated with the thermo-mechanical bond–slip curves varying at different temperatures. Various temperatures at the bond interface of 20°C, 23°C, 48°C, 70°C, 89°C, 107°C, and 123°C are examined. The results obtained from the developed bond model for the ETS-GFRP bar-to-concrete joint at elevated temperature show similar trend with those achieved from the FEM simulation with the developed thermo-mechanical bond–slip model. The bond fracture energy (G_{fT}) and ductility index (B_{fT}) govern the bond response of the ETS-GFRP bar–concrete interface at elevated temperature. When the thermal loading is below the glass transition temperatures of the GFRP bar and adhesive, a slight reduction in the bond stiffness and capacity is observed by the thermo-mechanical bond–slip model. The degradation in bond performance is significant at high temperature levels. The bond force, interfacial shear stress, and strain due to the mechanical loading have opposite directions to those due to thermal loading.

1. Introduction

Following the development of multi-disciplinary science, the appropriate combination of various systems and materials, which are the governances of distinct fields, to obtain good and innovative solutions for specific problems has become necessary. For example, the use of fiber-reinforced polymer (FRP) composites, which are well-known materials in the aerospace industry, for the retrofit of reinforced concrete (RC) structures is one of the most impressive solutions [1–8]. Common FRP materials include glass FRP (GFRP), aramid FRP (AFRP), basalt FRP (BFRP), and carbon FRP (CFRP). Much research and many practical applications have demonstrated the effectiveness of employing FRP sheets, laminates, plates, and bars to adhere onto concrete surfaces to improve or restore the performance of the RC members [1–3] (i.e., external bonding (EB) and near-surface mounted (NSM) methods). A new strengthening method named embedded through-section (ETS) has recently been developed by several research groups [2, 9–14]. The ETS method uses steel, FRP bars or laminates adhesively embedded into holes that are pre-drilled through the beam height in the shear zone of the RC beam.

*Corresponding authors: chihieuma@hcmut.edu.vn
[a]orcid.org/0000-0003-1178-4907; [b]orcid.org/0000-0003-4680-2466
DOI: http://dx.doi.org/10.17515/resm2026-1469me0115rs

Bond behavior between the strengthening element and concrete plays an important role in the efficiency of the intervention methods. If the FRP–concrete joint was debonded, then cracks in the concrete would rapidly develop and open, which would lead to earlier failure [15]. Many studies [16–19] related to the interfacial profile between EB-FRP or NSM-FRP composites and concrete were conducted. The guidelines for the design of strengthening systems for existing structures have since been provided by national and international associations, such as the American Concrete Institute (ACI PRC-440.2-17) [20], the Japan Society of Civil Engineers (JSCE 2007) [21], the Canadian Standards Association (CSA 2012) [22], and the International Federation for Structural Concrete (fib bulletin 2019) [23]. Aside from mechanical issues, the impact of fire on the FRP composite-to-concrete bonded joints should be considered. To address this issue, Gao et al. [24] and Dai et al. [25] presented analytical modeling of the bond behavior between EB-FRP laminate and concrete at elevated temperature. In their studies, the temperature variable was considered and coupled into the solutions of the governing equation. Their proposed bond models have been carefully verified with accessible experimental data. These researchers indicated that the elevated temperature had a noticeable effect on the bond performance between EB-FRP laminate and concrete. No clear difference in the bond–slip response was observed when the temperature at the bond interface was increased to 40 °C. The bond strength became small and the slip became large as the temperature at the bond interface was larger than 55 °C; therefore, the adhesive began the softening phase at 55 °C. The bond capacity seemed to be almost disappeared when the temperature was over 100 °C. These findings imply that the bond mechanism between EB-FRP laminate and concrete is quickly degraded at elevated temperature. The EB-FRP laminate–concrete interface is susceptible to high temperature due to its close-contact to the elevated temperature source and the nature of FRP and the thermal properties of the adhesive materials, and it would thus deteriorate early. However, it can be visualized that the ETS-FRP bar embedded into the core of a concrete prism would isolate the ETS-FRP bar from the temperature agent. The temperature at the ETS-FRP bar–concrete interface can be identified via the heat transfer mechanism from the concrete surface to the center of bar.

Realizing the benefits of the ETS strengthening method, particularly in terms of the bond mechanism, Godat et al. [26], Caro et al. [27], and Bui et al. [15, 28, 29] investigated the interfacial profile between ETS-FRP bar and concrete using experiments and modeling. Bui et al. [15, 28, 29] developed a nonlinear bond model, which was based on the original bond model proposed by Dai et al. [18]. The bond model contains two key bond parameters, the interfacial fracture energy (Gf) and bond ductility index (B), which physically and analytically govern the properties of the ETS-FRP bar-to-concrete bonded joint. Based on experimental and theoretical analyses, the structural efficiency of the members with ETS-FRP bar–concrete joints were determined to outperform those with EB-FRP or NSM-FRP composite–concrete joints. Furthermore, Bui et al. [28] conducted a parametric investigation of the ETS-FRP bar-to-concrete bonded joint using the finite element method (FEM). Their study successfully proposed effective bond length and bond force equations based on the FE analyses. In addition, the tendency of various effects, such as concrete compressive strength, FRP type, bonded length, and adhesive properties, on the performance of the ETS bonding technology was consistent with EB and NSM bonding in terms of the trend of those effects on the adhesion performance. However, the bond properties of ETS-FRP bar-to-concrete interfaces subjected to elevated temperature have not been investigated in any past works. Understanding of the bond performance between ETS-FRP bar and concrete at elevated temperature could open new insights into the practical application of the ETS method for the strengthening of existing RC structures damaged by fire.

This study aims to theoretically examine the effect of elevated temperature on the bond behavior of the ETS-GFRP bar-to-concrete bonded joint. To this end, the reliable bond–slip model initially proposed by Bui et al. [15] for the ETS-GFRP bar-to-concrete bonded joint at ambient temperature is theoretically developed to include the temperature variable. Then, the FE model for the ETS-GFRP bar-to-concrete bond interface is established with the developed thermo-mechanical bond–slip bond–slip law. The results from the analysis using the analytical bond model for the ETS-GFRP bar-to-concrete bonded joint at elevated temperatures are compared with those obtained from FEM modeling.

2. Materials And Methods

2.1 Bond–Slip Model

Based on the force equilibria illustrated in the free body diagram shown in Fig. 1, the governing equations of strain [$\varepsilon(x)$] and bond stress [$\tau(x)$] related to the slip variable [$s(x)$] for the bond problem of ETS bar adhered to concrete are presented in Eqs. (1a) and (1b). It should be noted that the governing equations have been furnished elsewhere by the authors [15, 29].

$$\varepsilon(x) = \frac{ds(x)}{dx} \tag{1a}$$

$$\tau(x) = \frac{E_r A_r}{(1+\alpha)\, p_r} \frac{d\varepsilon(x)}{dx} = \frac{E_r A_r}{(1+\alpha)\, p_r} \frac{d^2 s(x)}{dx^2} \tag{1b}$$

where E_r is the elastic modulus of the ETS bar (GPa), A_r is the cross-sectional area of the ETS bar (mm^2), p_r is the perimeter of the ETS bar (mm), α is the stiffness ratio of the ETS bar to the concrete, i.e., $E_rA_r/p_rE_ct_cb_c$, where E_c is the elastic modulus of the concrete (GPa), and t_c and b_c are the thickness and width of the concrete block (mm), respectively, for simplicity, $t_c = c/2$ and $b_c = c$.

By developing the original bond–slip model proposed by Dai et al. [18] for assessment of the bond behavior between EB-FRP sheet and concrete, Bui et al. [28] established the nonlinear strain–slip law, which is followed by the bond–slip rule after substituting the strain–slip relationship to Eqs. (1a) and (1b), to analyze the interfacial response of the ETS-FRP bar-to-concrete bonded joint, as shown in Eqs. (2a) and (2b). The analytical bond model is governed by two key parameters that represent the interfacial fracture energy (G_f) and bond ductility index (B). The interfacial fracture energy (G_f) is directly related to the maximum strain in the ETS-FRP bar (A) via Eq. (2c). The physical meaning of the interfacial fracture energy (G_f), which is defined by the area underneath the bond stress slip curve, is the debonding capacity of the bonded joint. The bond ductility index (B) represents the stiffness and bond strength reduction (descending branch of the bond–slip curve).

$$\varepsilon = A(1 - e^{-Bs(x)}) \tag{2a}$$

$$\tau = A^2 B \frac{E_r A_r}{(1+\alpha)\, p_r} e^{-Bs(x)} (1 - e^{-Bs(x)}) \tag{2b}$$

$$\therefore G_f = \int_0^{s_u} \tau ds = \frac{E_r A_r}{p_r (1+\alpha)} \times A^2 \times \left(\frac{1}{2} e^{-2 s_u B} - e^{-s_u B} + \frac{1}{2} \right) \tag{2c}$$

Fig. 2 depicts the curve fitting of the analytical formulation to the experimental data for the slip–strain relationships at the loaded end and at a location far away from the loaded end by 30 mm for the ETS-pullout test specimen C6 in the study of Bui et al. [28]. The engineering information of the ETS-pullout specimen C6, which is sketched in Fig. 1, was as follows: concrete block size = 150 × 150 × 250 mm, concrete compressive strength f'_c = 38 MPa, bonded length L_e = 250 mm, ETS-GFRP bar diameter d_b = 10 mm, elastic modulus of GFRP bar E_r = 50 GPa, tensile strength of GFRP bar f_{fu} = 1076 MPa, hole diameter d_h = 15 mm, elastic modulus of adhesive E_a = 4 GPa, and tensile strength of adhesive f_a = 21 MPa. The strain–slip relationship at the loaded end determined from the test data is fitted very well with the strain–slip curve plotted by the analytical model. The bond parameters after the curve fitting of the strain versus slip at the loaded end are G_f = 5.67 (N/mm) and B = 2.5 (1/mm). The coefficient of determination (R^2) for the curve fitting of the strain versus slip is larger than 0.95. In addition, Bui et al. [28] applied the curve fitting for the strain–slip relationship at the location far away from the loaded end by 30 mm. They found that the bond parameters G_f = 1.17 (N/mm) and B = 8.7 (1/mm) provided the best fit to the experimental measurement. These values are reasonable because less bond fracture energy (G_f) gives a larger

bond ductility index (B) (i.e., the smaller ductility), which are the physical meanings of the G_f and B terms defined in the bond model. As shown in Fig. 2, the bond parameters have a noticeable influence on the results of the strain versus slip relationships, in which the increase of G_f enhances the strain capacity, while the increase of B reduces the ductility. Evaluation of the bond–slip model is presented in the next section.

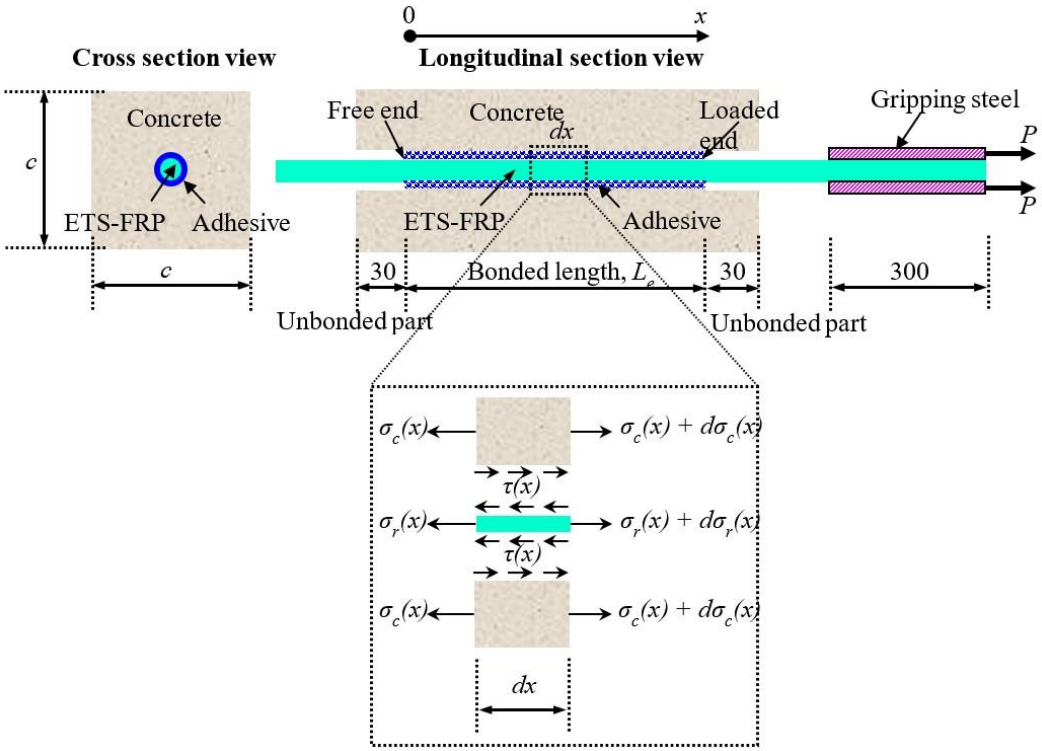

Fig. 1. Free body diagram for ETS-FRP bar bonded to concrete under a loading condition (dimensions in millimeters)

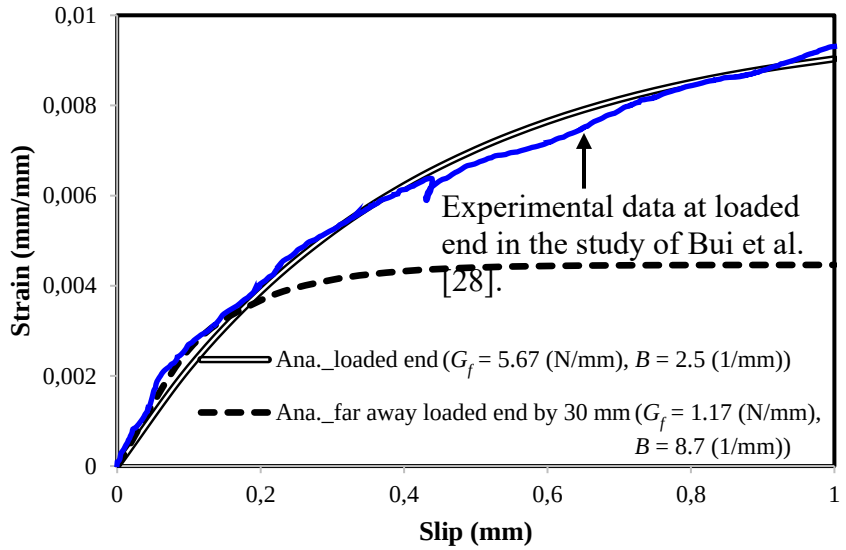

Fig. 2. Curve fitting of analytical model to available test data.

Substituting Eq. (2a) into Eq. (1a), the exact solution to Eq. (1a) is expressed as:

$$s(x) = \frac{1}{B}\ln\left[e^{B(Ax+c)} + 1\right] \tag{3}$$

Substituting Eq. (3) into Eq. (1a) and Eq. (1b) yields the following equations:

$$\varepsilon(x) = A \times \frac{e^{B(Ax+c)}}{e^{B(Ax+c)}+1} \tag{4}$$

$$\tau(x) = A^2 B \times \frac{E_r A_r}{p_r(1+\alpha)} \times \frac{e^{B(Ax+c)}}{\left[e^{B(Ax+c)}+1\right]^2} \tag{5}$$

The boundary condition is determined by the strain at the loaded end $\varepsilon(L_e) = P/(E_r A_r)$, in which P is the pullout force. Substituting this boundary condition into Eq. (4), the constant c can be written as:

$$c = \frac{\ln \frac{P/P_{\max}}{1-P/P_{\max}}}{B} - AL \tag{6}$$

2.2 Bond Model Of ETS-GFRP Bar-To-Concrete Bonded Joint at Elevated Temperature

In Fig. 3, the temperature on the surface of the concrete specimen is indicated by T °C. According to the heat transfer mechanism, the temperature obtained at the interface of the ETS-GFRP bar to the concrete is $T_{interface}$ °C. A simplified empirical formulation is adopted to estimate the bond interface temperature. This approach captures the dominant heat transfer behavior but does not account for temperature-dependent concrete degradation, thermal cracking, or adhesive changes during heating. The temperature at the bond interface via the heat transfer distribution in the concrete covering is derived from an empirical formulation proposed by Abbasi and Hogg [30]:

$$T = 345\log(8t+1) + 20 \tag{7a}$$

$$T_{interface} = 345\log(8t+1) + 20 - 767\exp^{-0.001\exp(7.602/c - 23.623)t} \tag{7b}$$

where t is the time subjected to the temperature agent (minutes), and c is the concrete cover thickness (mm).

According to the assumption, the primary effects on the interfacial profile between the ETS-GFRP bar and concrete are governed by the changes of the bond parameters (G_f, B) due to the elevated temperature. Under temperature variation, the original interfacial fracture energy and bond ductility index represented in the bond model at ambient temperature ($T_{ambient}$ is assumed to be 20 °C) are denoted as G_{f0} (N/mm) and B_{f0} (1/mm). The interfacial fracture energy and bond ductility index at an elevated temperature are denoted as G_{fT} (N/mm) and B_{fT} (1/mm). Conversely, the remaining elastic modulus of the ETS-GFRP bar at the elevated temperature is defined as E_{rT} (GPa).

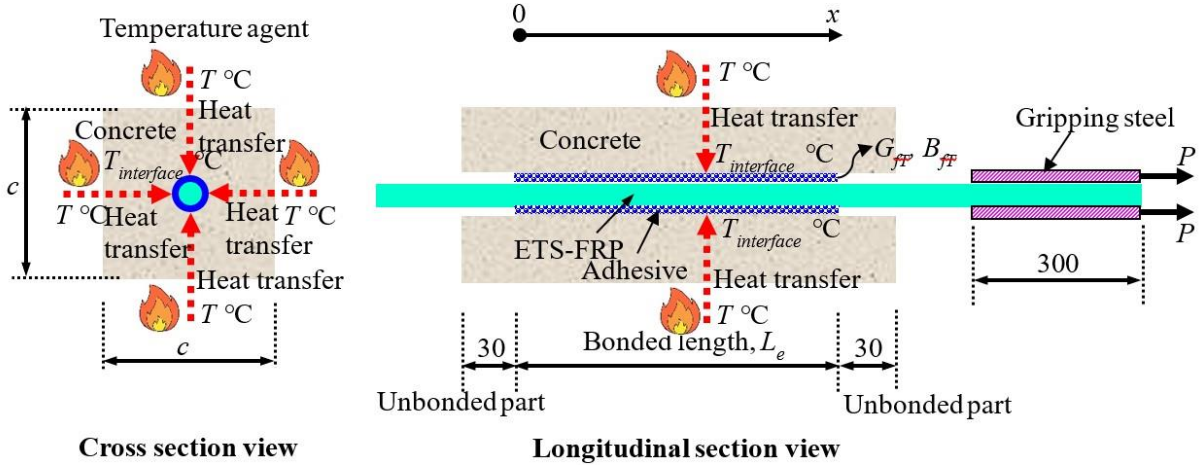

Fig. 3. Schematic diagram of the effect of temperature at the ETS-GFRP bar-to-concrete interface (dimensions in millimeters)

Gao et al. [24] and Dai et al. [25] presented the expression of the constant c with consideration of the temperature variable, in which two components of strain by mechanical and thermal deformation are incorporated. The temperature variable at the interface is considered by the temperature variation ($\Delta T = T_{interface} - T_{ambient}$). ΔT is required to determine the thermal expansion at the interface. Thereby, Eq. (6) yields to Eq. (8):

$$c = \frac{1}{B_{fT}} \ln \frac{\frac{1}{A}\left[\frac{P(1+\alpha)}{E_{rT}A_r} + (\alpha_r - \alpha_c)\Delta T\right]}{1 - \frac{1}{A}\left[\frac{P(1+\alpha)}{E_{rT}A_r} + (\alpha_r - \alpha_c)\Delta T\right]} - AL \tag{8}$$

where B_{fT} is the bond ductility index at $T_{interface}$ °C (1/mm), E_{rT} is the elastic modulus of GFRP bar at $T_{interface}$ °C (GPa), α_r is the thermal expansion coefficient of GFRP bar, taken as 33×10^{-6} (mm/mm/°C), and α_c is the thermal expansion coefficient of concrete, taken as 8×10^{-6} (mm/mm/°C). The strain that occurs in the ETS-GFRP bar includes the mechanical deformation and thermal expansion. Therefore, the pull load that occurs on the ETS-GFRP bar is determined by:

$$P(x) = \frac{E_{rT}A_r}{(1+\alpha)}\left[\varepsilon(x) - (\alpha_r - \alpha_c)\Delta T\right] \tag{9}$$

When the slip in the ETS-GFRP bar reaches the ultimate slip (s_u), Eq. (9) becomes the ultimate pullout load and can be expressed as:

$$P_{uT} = \frac{E_{rT}A_r}{(1+\alpha)}\left[A\left(1 - e^{-B_{fT}s_u}\right) - (\alpha_r - \alpha_c)\Delta T\right] \tag{10a}$$

$$\therefore P_{uT} = \sqrt{\frac{2G_{fT}E_{rT}A_r p_r}{(1+\alpha)}} - \frac{E_{rT}A_r}{(1+\alpha)}(\alpha_r - \alpha_c)\Delta T \tag{10b}$$

where G_{fT} is the interfacial fracture energy at $T_{interface}$ °C (N/mm). Without loss of generality, the present study assumes that the normalizations for the elastic modulus of GFRP bar (E_{rT}/E_r), interfacial fracture energy (G_{fT}/G_{f0}), and bond ductility index (B_{fT}/B_{f0}) under the effect of temperature for the ETS-FRP bar-to-concrete bonded joint are identical with the corresponding terms for the EB-FRP laminate-to-concrete bonded joint. Further, the temperature-dependent relationships adopted from externally bonded FRP systems are considered applicable to ETS systems because they are governed by intrinsic material degradation mechanisms (e.g., resin softening and interfacial weakening), which are largely independent of strengthening configuration. In the absence of ETS-specific models, this represents a reasonable and conservative assumption. Therefore, the empirical regression formulations for the elastic modulus of FRP, interfacial fracture energy, and bond ductility index established in the study by Dai et al. [25] are utilized to identify the material and bond parameters for the ETS-FRP bar–concrete interface at an elevated temperature. The normalized equations for the elastic modulus, interfacial fracture energy, and bond ductility index with consideration of the thermal loading are:

$$\frac{E_{rT}}{E_r} = \left(\frac{1-a_1}{2}\right) \times \tanh\left[-a_2 \times \left(\frac{T}{T_{g,b}} - a_3\right)\right] + \left(\frac{1+a_1}{2}\right) \tag{11a}$$

$$\frac{G_{fT}}{G_{f0}} = \frac{1}{2} \times \tanh\left[-b_2 \times \left(\frac{T}{T_{g,a}} - b_3\right)\right] + \frac{1}{2} \tag{11b}$$

$$\frac{B_{fT}}{B_{f0}} = \left(\frac{1-c_1}{2}\right) \times \tanh\left[-c_2 \times \left(\frac{T}{T_{g,a}} - c_3\right)\right] + \left(\frac{1+c_1}{2}\right) \quad (11c)$$

where a_1 = 0.729, a_2 = 9.856, a_3 = 0.607, b_2 = 3.206, b_3 = 1.313, c_1 = 0.485, c_2 = 14.053, and c_3 = 0.877 are the empirical factors identified based on a regression analysis of the available data collected by Dai et al. [25], $T_{g,a}$ is the glass transition temperature of the adhesive, taken as 62 °C [25], and $T_{g,b}$ is the glass transition temperature of the GFRP bar, taken as 55 °C [25]. The empirical models for E_{rT}, G_{fT}, and B_{fT} has been sufficiently formulated in the work of Dai et al. [25].

The bond shear stress and strain distributions at elevated temperature can be determined by substituting the values obtained from the constant c [Eq. (8)], elastic modulus E_{rT} [Eq. (11a)], interfacial fracture energy G_{fT} [Eq. (11b)], and bond ductility index B_{fT} [Eq. (11c)] into Eqs. (4) and (5).

2.3 Finite Element Method

A number of efficient FE analyses were performed to study the bond behavior between EB-FRP composite and concrete, for example, Shi et al. [31] and He et al. [32]. Bui et al. [15] conducted FEM simulations with the ANSYS 15.0 (ANSYS 2013) [33] package to investigate the interfacial profiles of the ETS-FRP bar-to-concrete bonded joint. Their study examined the trapezoidal bond law to analyze the interaction between ETS-FRP bar and concrete. The nonlinear bond rule, which was developed in a past study by Bui et al. [28], was not considered in the work of Bui et al. [15]. The present study uses the FE models for the specimens named C2-1.5d-9.5S-20d, C2-1.5d-9.5S-25d, C2-1.5d-9.5S-30d, and C6, which were built in the work of Bui et al. [15]. Additionally, these FEM simulations adopt the nonlinear bond rule described in section 2, which aim to compare with the FE models analyzed in Bui et al. [15]'s study.

To incorporate the temperature effect on the bond interface, the bond–slip curve used in the FEM modeling was defined for different temperature levels based on the degradation laws of the parameters given in Eqs. (11a)–(11c). In the ANSYS 15.0 (ANSYS 2013) [33] program, the element models for concrete, ETS-GFRP bar, and interfacial interaction are SOLID65, LINK180, and COMBIN39, respectively. The SOLID65 element has three degrees of freedom at each node of an eight-node brick. The LINK180 element represents a two-node bar with three degrees of freedom at each node. The COMBIN39 element is represented by a nonlinear spring, which is characterized by the load–displacement relationship (i.e., related to the bond response). The displacement control is applied in the FEM simulation.

The constitutive material law of concrete in compression employs the equation offered in the study of Hognestad et al. [34], as illustrated in Fig. 4(a), and is expressed by Eq. (12). The kinematic hardening option (KINH) is used to include the plasticity of concrete in the FE analysis. In addition, the model of concrete under tension is demonstrated in Fig. 4(b), which is available in ANSYS 15.0 (ANSYS 2013) [33]. The tensile strength of concrete is taken as $0.6\sqrt{f_c^{'}}$ (MPa) [9]. A steep drop of 40% reduction in the tensile strength is assumed in the model to reflect the crack initiation and development. The descending branch then becomes gentler until the maximum strain is equal to six times of the strain at the peak strength. The post-cracking stiffness of the concrete element is defined by R^t. The open and closed shear transfer coefficients are β_t = 0.2 and β_c = 0.8, respectively, which were recommended by Bui et al. [15].

$$f_c = f_c^{'}\left[2\left(\frac{\varepsilon}{\varepsilon_0}\right) - \left(\frac{\varepsilon}{\varepsilon_0}\right)^2\right] \quad (12)$$

where $\varepsilon_0 = 2f'_c/E_c, E_c = 3300\sqrt{f_c^{'}} + 6900$ (MPa) [9], and the concrete is crushed when ε_u is larger than 0.0038.

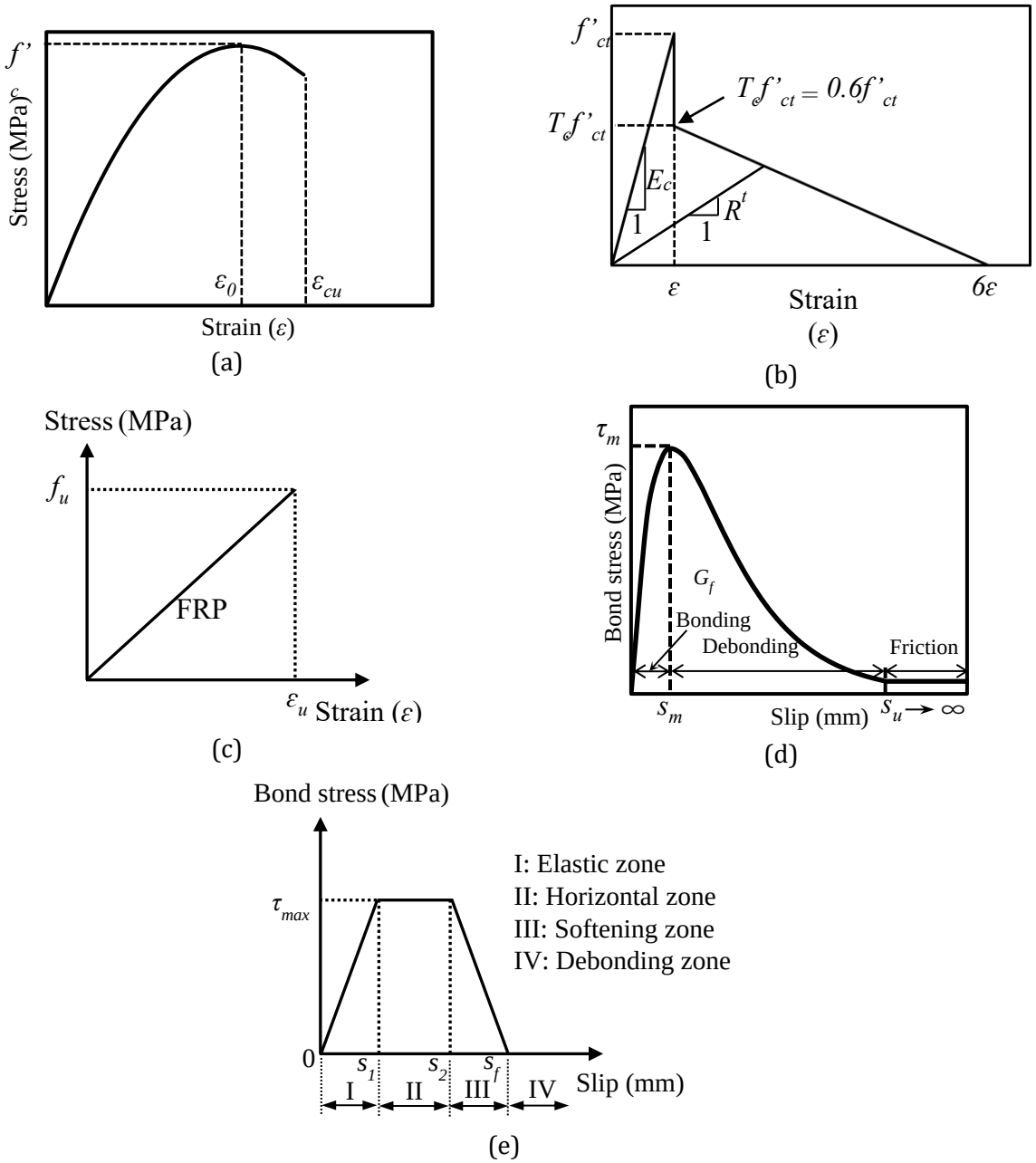

Fig. 4. Constitutive models for FE analysis: (a) concrete model under compression [15, 29]; (b) concrete model under tension [15, 29]; (c) FRP bar [15, 29]; (d) nonlinear bond model [28]; (e) trapezoidal bond model [15].

The constitutive material model of the GFRP bar is linear until rupture, as shown in Fig. 4(c). Fig. 4(d) shows the nonlinear law that represents the bond response at the ETS-GFRP bar-to-concrete interface. The bond–slip model is given in Eq. (2b). As revealed in Fig. 4(d), the nonlinear bond model developed by Bui et al. [28] captures the three main stages of the bond behavior, i.e., bonding, debonding, and friction. Moreover, the reliability of the nonlinear bond model has been verified with sufficient experimental data obtained from previous literature [9, 27–29]. Fig. 4(e) illustrates the trapezoidal bond law proposed in Bui et al. [15]'s study, which identifies the bond mechanism of ETS bar-concrete interface via four zones of elastic (I), horizontal (II), softening (III), and debonding (IV) zones. The COMBIN39 element requires the bond force–slip relationship; therefore, the bond stress–slip curve is converted to the bond force–slip curve. The bond force acting on a meshing element of the GFRP bar can be calculated as $\tau \times \pi \times d_r \times e$ (N), where τ is the bond stress (MPa), d_r is the bar diameter (mm), and e is the element size after meshing refinement (mm). Section 4.2 presents the details of the changes of the bond versus slip under the influence of temperature variation to reflect the bond degradation.

Fig. 5 shows a representative FE model established in ANSYS 15.0 (ANSYS 2013) [33] for the specimen C6 in the study by Bui et al. [28]. Bui et al. [15] selected the suitable meshing sizes which is 5 × 5 ×5 mm for the pullout specimens. The mesh density was selected to ensure stable and consistent results. The interface behavior is modeled using calibrated parameters based on established practices in the literature. While a detailed mesh convergence and sensitivity analysis is beyond the scope of this study, the adopted modeling approach provides a reasonable representation of the bond behavior. The important information involving specimen C6 and its FE model is presented in Fig. 5 and is summarized in section 2.1 and Table 1. These details can also be found elsewhere in the study of Bui et al. [15].

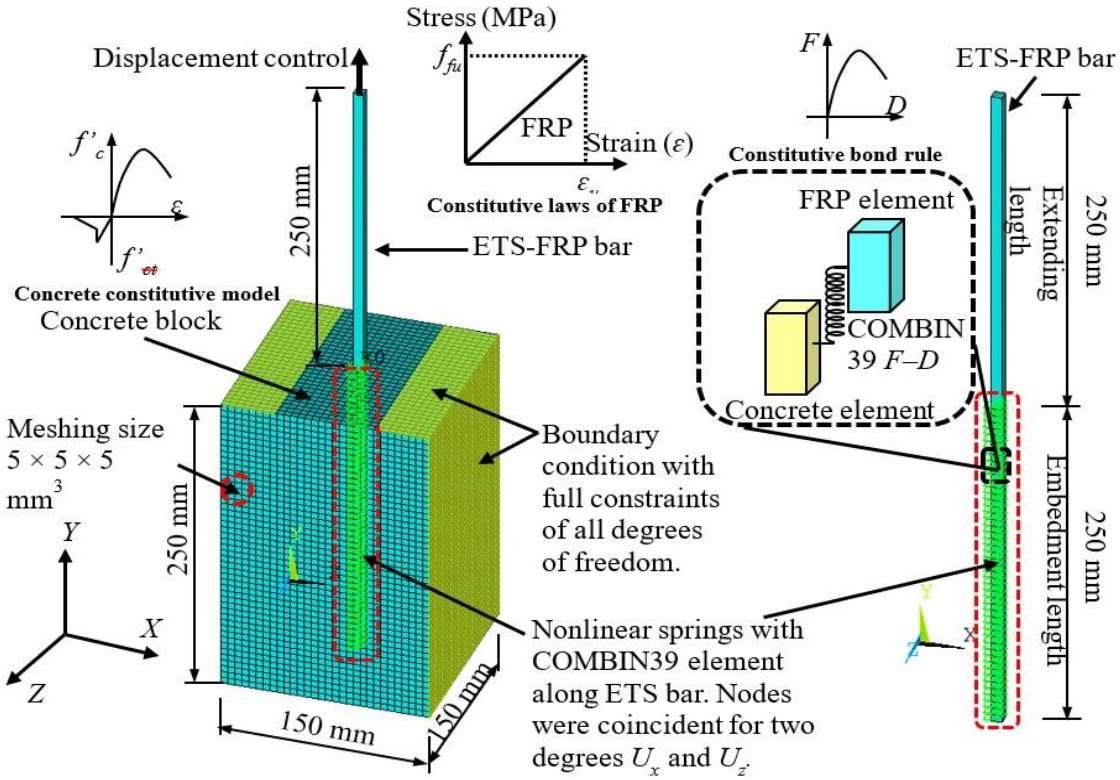

Fig. 5. A FE model for the pullout specimen C6 to investigate the bond behavior between ETS-GFRP bar and concrete [15]

3. Results and Discussion

First, the reliability of the FEM simulation with developed bond model is evaluated. To this end, four pullout specimens, which were tested in past studies [26, 28], are numerically modeled. The FEM results with nonlinear bond model developed in this study are compared with those with trapezoidal bond law assessed in the numerical work of Bui et al. [15]. Both FEM results are corroborated to the experimental data and analytical approach proposed in section 2. After validating the FEM simulation, the analyses on the bond responses of ETS-FRP bars to concrete with elevated temperature at interface are implemented. The specimen details, bond factors, and pullout results achieved from experiments, FE models, and analytical modeling are summarized in Table 1.

Table 1. Specimen configurations and pullout load results

Study	Specimen label	Overall geometries	f'_c (MPa)	L_e (mm)	d_b (mm)	E_r (GPa)	f_{fu} (MPa)	G_f (N/mm)	B (1/mm)	$P_{Exp.}$ (kN)	P_{FEM} (trapezoidal bond law) (kN) [15]	P_{FEM} (nonlinear bond rule) (kN)	$P_{Ana.}$ (kN)
Godat et al. [26]	C2-1.5d-9.5S-20d	190 × 190 × 190	42.7	190	9.52	155	2800	15.89	69.3	102.4	106.2	100	102.2
	C2-1.5d-9.5S-25d	190 × 190 × 238	42.7	238	9.52	155	2800	19.65	69.3	114.7	125.1	121.4	113.7
	C2-1.5d-9.5S-30d	190 × 190 × 285	42.7	285	9.52	155	2800	24.87	69.3	128.3	132.9	132.9	127.9
Bui et al. [28]	C6	150 × 150 × 250	38	250	10	50	1076	5.67	2.5	37.4	39.8	37.3	34.3

Notes: Overall geometries are defined by concrete prism width (mm) × concrete prism height (mm) × bonded length (mm), f'_c = concrete compressive strength (MPa), L_e = embedment (bonded) length (mm), d_b = ETS bar diameter (mm), E_r = elastic modulus of ETS bar (GPa), f_{fu} = tensile strength of ETS bar (MPa), G_f = bond fracture energy (N/mm) defined by the developed bond model, B = bond ductility index (1/mm) defined by the developed bond model, $P_{Exp.}$ = maximum pullout force obtained from the experiments (kN), P_{FEM} (trapezoidal bond law) = maximum pullout force obtained from FE models with trapezoidal bond law determined in the study of Bui et al. [15] (kN), P_{FEM} (nonlinear bond rule) = maximum pullout force obtained from FE models with nonlinear bond rule in the present study (kN), $P_{Ana.}$ = maximum pullout force obtained from analytical model based on nonlinear bond rule developed in the present study (kN). Note that the bond factors (G_f, B) are determined through the calculations of the results from relevant pullout tests to the analytical equations of G_f and B in the developed bond model.

3.1 Comparison of FEM and analytical modeling against experiments at ambient temperature

Obviously, Figs. 6(a)−(d) reveal that the FEM simulations and analytical modeling show reasonable numerical agreement with the pullout test data in terms of load versus slip relations for all four specimens. The maximum discrepancy at the peak bond force between predicted (i.e., FEM and analytical modeling) and experimental values among four specimens is less than 10%, which can be derived from the maximum load results depicted in Table 1. The adhesion quality of the bonded joints, for example, the discontinuity of adhesive injection, in the pullout specimens might affect the bond behavior, leading to the difference between numerical models and experiments. Additionally, the strain gauges attached on the ETS-FRP bars of the bonded joints investigated in Bui et al. [28]'s study resulted in the partial disappearance of the adhesion.

Compared to the experimental observation, Figs. 6(a)−(d) reveal the FEM simulations and analytical computation rationally identified the debonding phases that were defined by the noticeable changes in the curve slopes occurred in four ETS-FRP bonded joints. In general, considering whole ranges of the pullout load−slip curves of four specimens in Figs. 6(a)−(b), the FE analyses and analytical modeling with nonlinear bond rule demonstrate the better predictions against the experimental results than the FE analyses with trapezoidal bond model examined in the numerical work of Bui et al. [15]. This is attributable to the nonlinear bond rule that was initially established based on the measured nonlinear strain distribution along the bond interfaces of the pullout tests. Meanwhile, the trapezoidal law was derived based on the fracture energy (G_f) related to the adhesive properties [15].

Conversely, three specimens of C2-1.5d-9.5S-20d, C2-1.5d-9.5S-25d, and C2-1.5d-9.5S-30d in Figs. 6(a)−(c) had different bonded lengths by 190 mm, 238 mm, 285 mm labeled with the suffixes of 20d, 25d, and 30d, respectively. All numerical and experimental results consistently demonstrate that the increase of bonded length led to the enhancement of peak bond force because the larger strain length resisted the greater force transfer. In Fig. 6(d), because of low elastic modulus, the experiments, FEM, and analytical modeling consistently indicate that the ETS bond specimen C6 employed the GFRP bar furnished the larger interfacial slip and smaller interfacial stiffness than those of other specimens (Figs. 6(a)−(c)) adopted the CFRP bars.

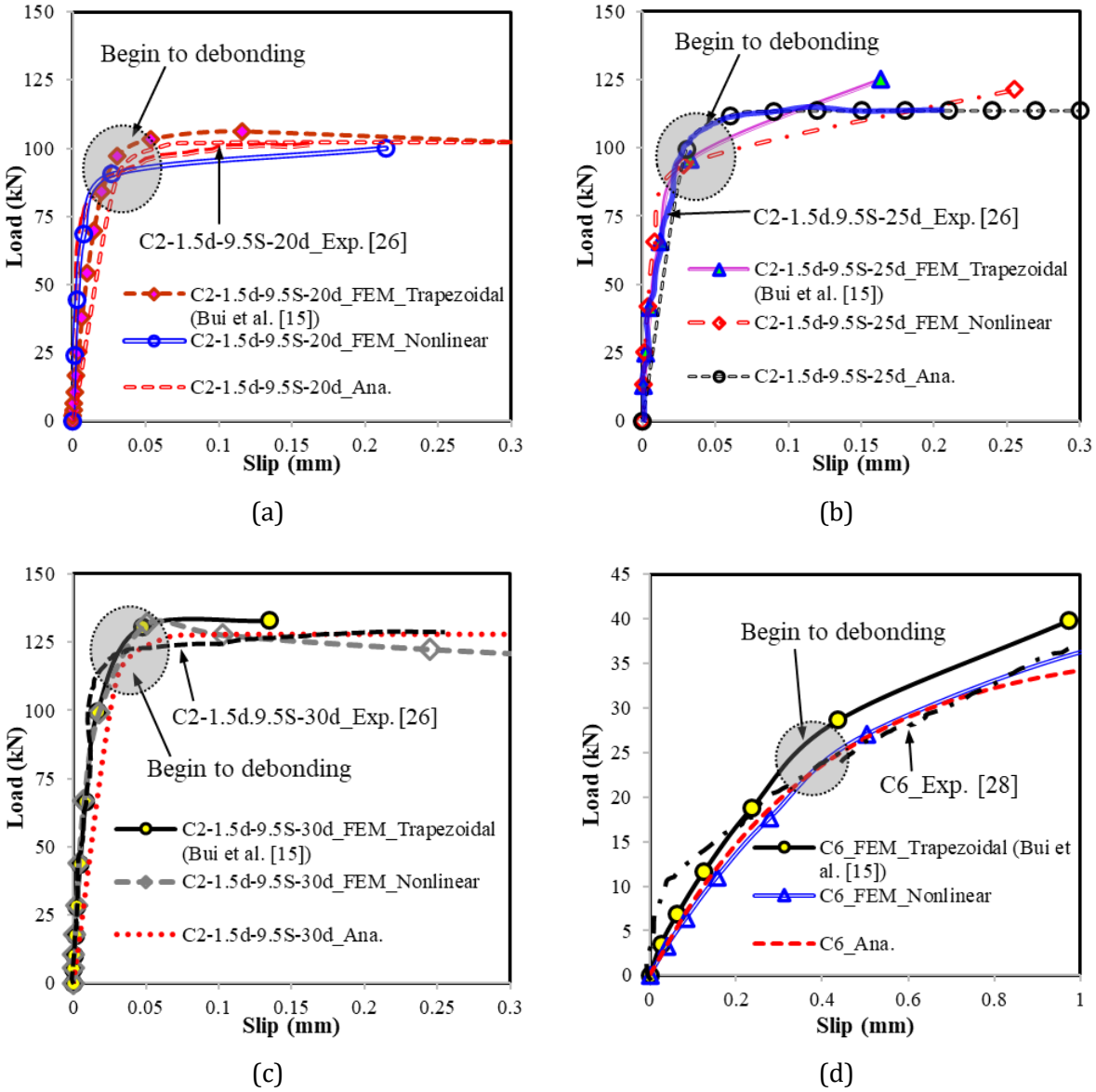

Fig. 6. Comparison of FEM and analytical modeling on load versus slip curves of specimens: (a) C2-1.5d-9.5S-20d; (b) C2-1.5d-9.5S-25d; (c) C2-1.5d-9.5S-30d; (d) C6

Note that the proposed thermo-mechanical bond–slip model has not been directly validated against experimental data at elevated temperatures due to the limited availability of experimental studies on ETS-GFRP bonded joints under thermal conditions. The experimental data used for evaluation in this study correspond to ambient temperature bond behavior reported in the literature. Therefore, the elevated temperature predictions presented in the following sections should be interpreted as analytical–numerical estimations rather than fully experimentally validated results. The FE simulations were used to provide a comparative numerical verification of the proposed model; however, both analytical and numerical approaches rely on similar material degradation assumptions at elevated temperatures.

3.2 Bond Stress Versus Slip Subjected to Elevated Temperature at Interface

Bond stress–slip curves for the interfacial profiles of the ETS-GFRP bar-to-concrete joint of specimen C6 at elevated temperature with two cases of the key bond features [G_{f0} (N/mm), B_{f0} (1/mm)] = (5.67, 2.5) and (1.17, 8.7) (shown in section 2.1) are shown in Figs. 7(a) and (b), respectively. Further, Fig. 7(b) demonstrates the validity of the bond slip plotted by the model to that derived from the test results given in Bui et al. [28]. Note that the available experiment only investigated the bond behavior of the ETS-GFRP bar-to-concrete joint at ambient temperature. As

observed in both Figs. 7(a) and (b), the bond–slip response at the ETS-GFRP bar–concrete interface begins to be decreased as the temperature at the interface increased up to $T_{interface}$ = 48 °C because the temperature at the interface was less than the glass transition temperatures of the adhesive ($T_{g,a}$ = 62 °C) and the GFRP bar ($T_{g,b}$ = 55 °C). However, a substantial reduction in the bond–slip curve in the ascending bond stiffness and capacity is observed when the temperature at the interface reaches $T_{interface}$ = 70 °C. The post-peak branches of the bond–slip curves become gentle as the temperature at the interface increases. Such observation is appropriate to the physical mechanism monitored from the pullout tests in the work of Dai et al. [18].

The physical meaning of the bond performance degradation predicted by the model is well suited to the actual bond behavior of FRP bars embedded in concrete. When heating a GFRP bar-to-concrete joint at an elevated temperature, the hard and brittle states of the GFRP bar and the bond interface gradually transit into a viscous phase, which softens the adherence capability of the ETS-GFRP bar to concrete. The formulations for the elastic modus of the GFRP bar (E_{fT}), the bond fracture energy (G_{fT}), and the bond ductility index (B_{fT}) reflected well the aforementioned phenomenon.

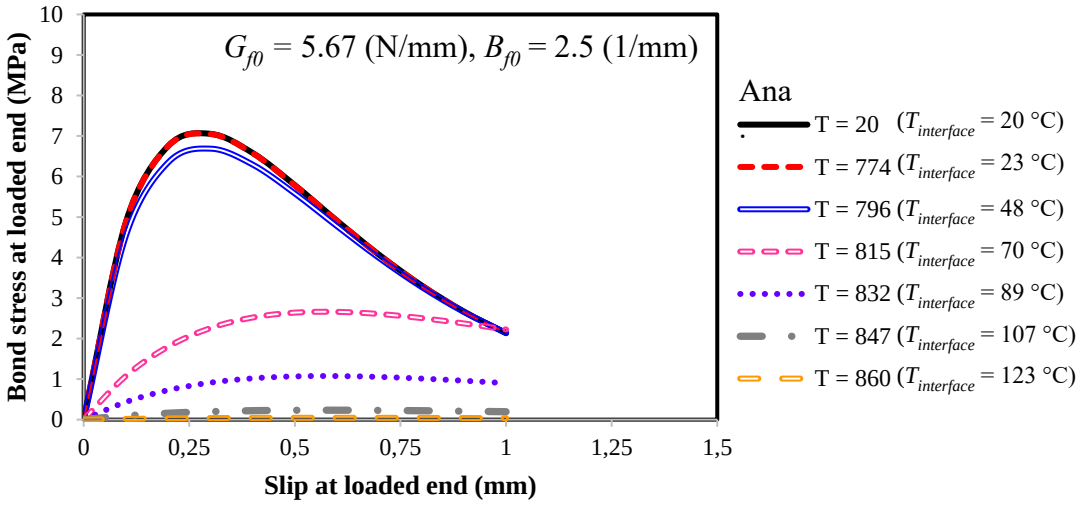

(a)

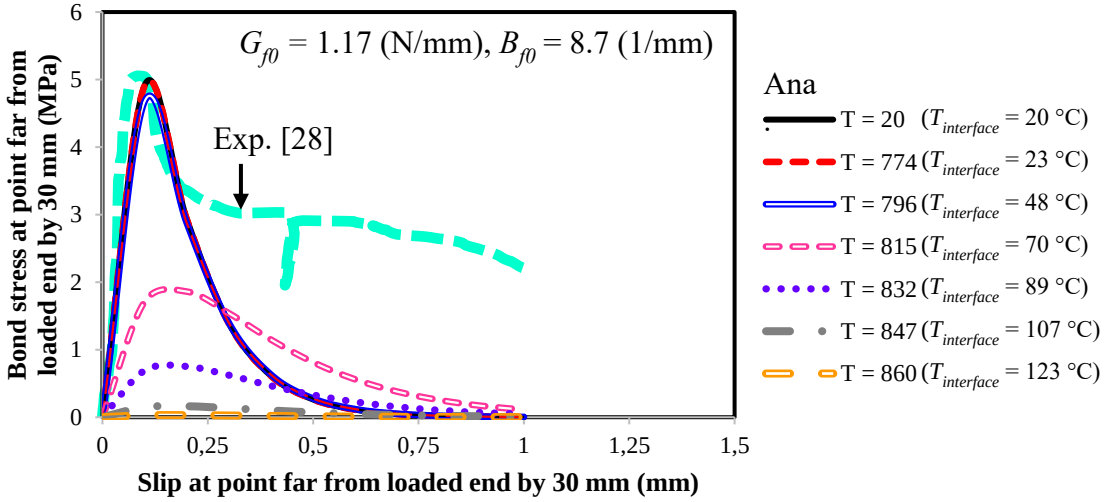

(b)

Fig. 7. Bond stress–slip relationship at elevated temperature of specimen C6: (a) Gf0 = 5.67 (N/mm) and Bf0 = 2.5 (1/mm) for loaded end; (b) Gf0 = 1.17 (N/mm) and Bf0 = 8.7 (1/mm) for location far away loaded end by 30 mm

3.3 Pullout Load and Slip Responses Subjected to Elevated Temperature at Interface

For two cases of bond factors, G_{f0} and B_{f0}, Fig. 8(a) shows the reduction of the maximum pullout load under the increase of temperature variation at the ETS-GFRP-bar–concrete interface of the specimen C6. This result is generally consistent with that predicted by the FE models. The bond force defined in Eq. (10b) is composed of the residual mechanical properties at each temperature level and the corresponding thermal deformation. The elevated temperature analysis is conducted on a representative specimen (C6) to illustrate the influence of temperature on bond behavior. The results are therefore not intended to be generalized to all ETS configurations.

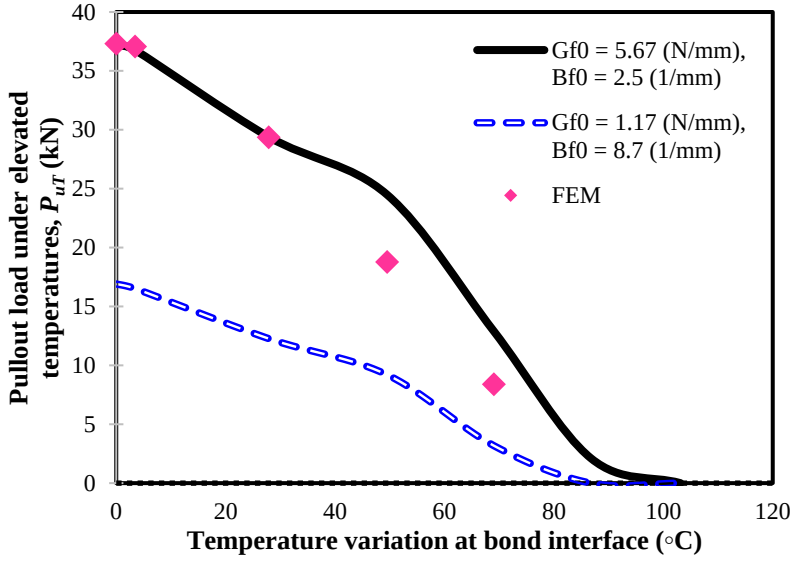

(a)

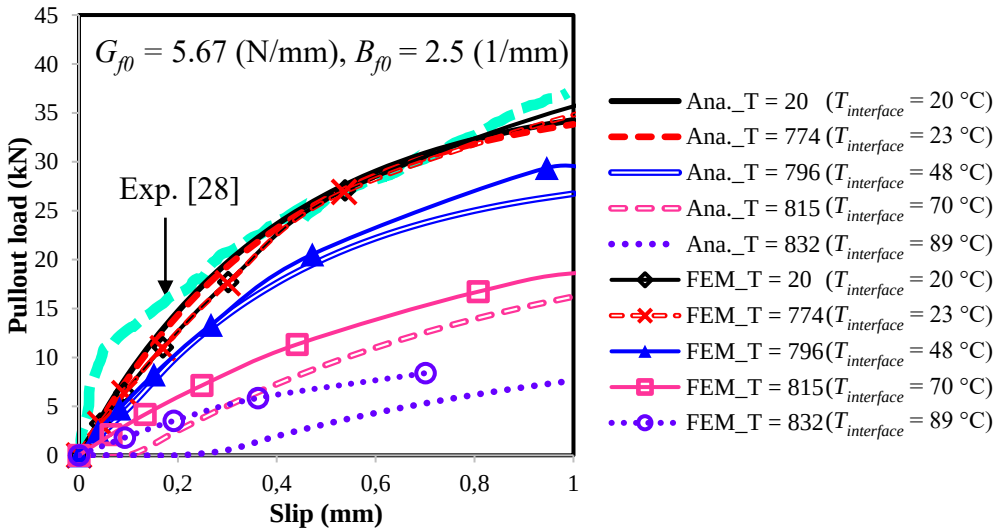

(b)

Fig. 8. Comparison of load versus slip at elevated temperature between test, analysis, and FEM of the specimen C6: (a) ultimate pullout load reduction; (b) pullout load–slip responses.

According to the results from the analytical computation, at ΔT = 45 °C (i.e., $T_{interface}$ = 65 °C), the slope in the pullout load reduction predicted by the model is gentle. This temperature level was slightly over the glass transition temperatures of the GFRP bar ($T_{g,b}$ = 55 °C) and the adhesive ($T_{g,b}$ = 62 °C). At this phase, both mechanical and thermal actions effectively resisted the pullout load, so that the degradation of the pullout load was slow. At high temperature variation, the bond force

predicted by Eq. (10b) degraded to 0 (kN), as indicated in Figs. 8(a) and (b). At very high temperatures, significant degradation of the adhesive, interface, and surrounding concrete leads to a loss of load transfer capability, and the bond resistance approaches zero. Any negative values predicted by the analytical model indicate complete bond failure rather than actual negative resistance. Accordingly, a lower bound of zero is adopted to ensure physical consistency. Such observations in the model are well suited to the actual behavior observed for EB-FRP laminate–concrete interface at elevated temperature in various pullout tests summarized by Dai et al. [25].

In Fig. 8(b), the bond force–slip responses of the ETS-GFRP–concrete interface obtained from the test, FEM, and analytical modeling for low temperature levels identify clearly three main stages of (I) elasticity, (II) bonding, and (III) friction. At higher temperatures, the pullout load–slip relationships plotted by the developed bond model could still capture the degradation of bond performance and could correspond well with the FE results. The discrepancy between the FE and analytical bond–slip responses becomes large as the temperature at the interface is over the glass transition limit of the GFRP bar, $T_{g,b}$ = 55 °C.

The degradation of bond behavior at elevated temperatures is governed by several physical mechanisms. Adhesive softening reduces the shear transfer capacity at the interface, while thermal expansion mismatch between the FRP bar, adhesive, and concrete induces additional stresses that weaken the bond. In addition, thermal-induced cracking in the surrounding concrete may further reduce confinement and load transfer capability. These mechanisms explain the reduction in bond strength and the changes observed in the bond–slip response and strain distribution.

3.4 Strain Distribution Along The ETS-GFRP Bar–Concrete Interface at Elevated Temperature

Fig. 9(a) shows the strain distribution along the ETS-GFRP bar–concrete adhered joint predicted by the FEM and analytical modeling for various temperatures exposed to the bond interface of the pullout specimen C6. The analytical results show similar trend with the FEM results at the ambient and medium temperature levels. At high temperatures, the strain development achieved from the bond model is larger than that obtained from the FEM modeling. The loads adopted at levels of $0.42P_u$ (11.34 kN), $0.76P_u$ (20.53 kN), $0.99P_u$ (26.91 kN), and $1P_u$ (27.09 kN), which represent the low, medium, and high load states, and are essential for the bond problem. The strain is distributed nonlinearly along the interface, in which the values of strain increased from the free end to the loaded end for the entire temperature range. At T = 20 °C and T = 774 °C, the strain profiles were similar because the receiving temperatures at the ETS-GFRP bar–concrete interface at these temperature levels were slightly different.

When the temperature was increased to T = 796 °C and T = 815 °C (i.e., the temperature at the bond interface was accordingly increased), the strain response along the ETS-GFRP bar-to-concrete bonded joint was significantly changed. The strain distribution is dependent upon the reduction of the elastic modulus of the ETS-GFRP bar and of the bond parameters (G_{fT}, B_{fT}) of the joint at elevated temperature. At T = 796 °C (i.e., $T_{interface}$ = 48 °C), the elastic modulus of GFRP bar was heavily reduced, while the bond parameters were gently decreased. Such a theoretical phenomenon makes the strain capacity of the ETS-GFRP bar to be highly developed. This result is feasible because $T_{interface}$ = 48 °C is close to the glass transition temperature of the GFRP bar ($T_{g,b}$ = 55 °C) but still less than the glass transition of the adhesive ($T_{g,a}$ = 62 °C).

However, at T = 815 °C (i.e., $T_{interface}$ = 70 °C, which is higher than the glass transition temperatures of the GFRP bar and adhesive), the elastic modulus of the GFRP bar and the bond parameters were significantly reduced, which led to a decrease of the deformability of the GFRP bar. Furthermore, at high temperature variation ($\Delta T = T_{interface} - T_{ambient}$ = 50 °C), the contribution of thermal deformation in the ETS-GFRP bar was noticeable, causing the non-zero value of the strain at the free end. Fig. 9(b) also shows the comparable results between the analytical modeling and FEM simulation in the strain distribution along the ETS-GFRP bar–concrete interface at T = 796 °C ($T_{interface}$ = 48 °C) under different pullout loads, particularly at the low and medium pullout forces. The increase of the pullout load results in an enhancement of the strain.

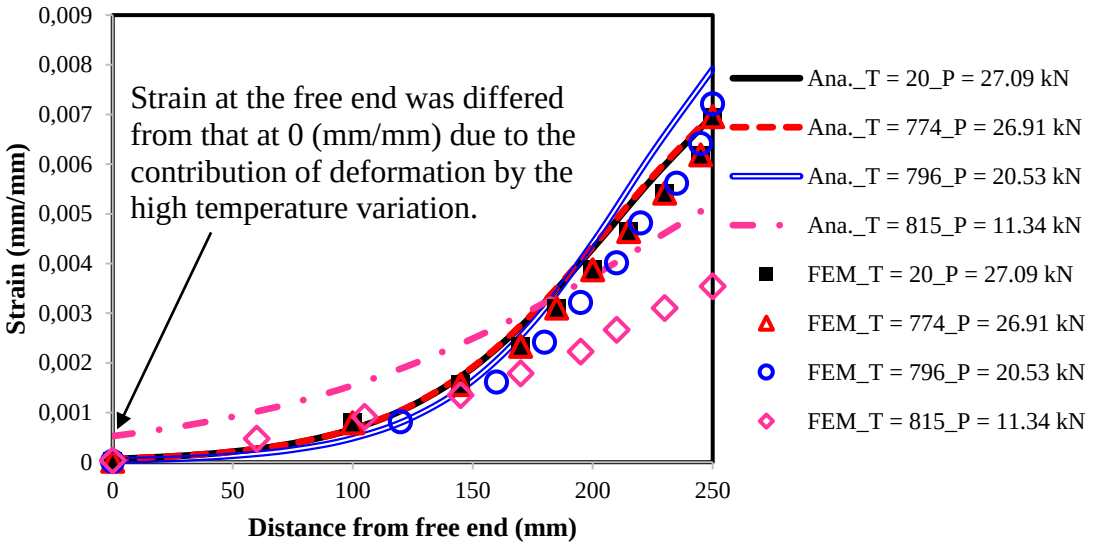

(a)

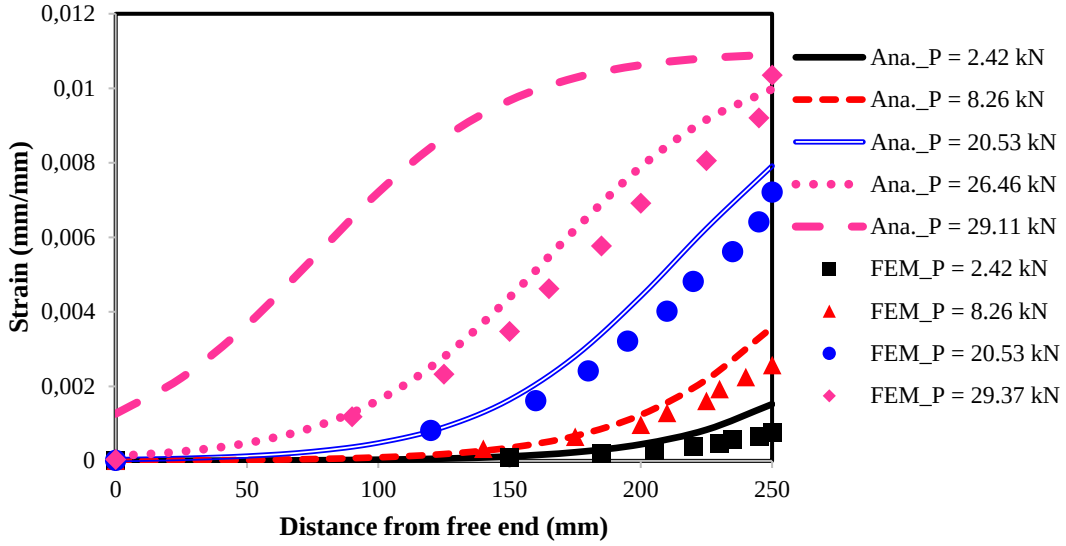

(b)

Fig. 9. Comparison between strain distributions obtained from analytical model and FE analysis of the specimen C6: (a) at elevated temperature; (b) at different pullout load levels at T = 796°C (Tinterface = 48 °C)

4. Conclusions

The primary conclusions can be summarized as follows:

- The combined variables of mechanical loading and elevated temperature were successfully captured in the developed bond model for the ETS-GFRP bar-to-concrete bonded joint. The proposed model was validated against available experimental data at ambient temperature, while the elevated temperature results should be considered as analytical–numerical predictions. Therefore, the applicability of the model at elevated temperatures should be interpreted within the limitations of the current study. The suitability of the developed bond model was compared with the available test data and FEM modeling in terms of the pullout load, slip, strain evolution, and bond shear stress distribution. Nevertheless, the assumption regarding temperature-dependent parameters should be further assessed through dedicated

experimental studies on ETS systems under elevated temperatures. More advanced coupled thermo-mechanical analyses are recommended for future research.

- The bond parameters of the interfacial fracture energy (G_{f0}, G_{fT}) and interfacial ductility index (B_{f0}, B_{fT}) significantly affected the bond responses between the ETS-GFRP bar and concrete subjected to both loading and elevated temperature. Based on the present results, the proposed model is expected to be more reliable at temperatures below or near the glass transition temperature range, where material degradation remains moderate. At higher temperatures, the predictions should be interpreted with caution due to significant material degradation and the assumptions adopted in the analytical and numerical models.
- The bond behavior of the ETS-GFRP bar–concrete interface was similar at temperatures below the glass transition temperature levels of the GFRP bar ($T_{g,b}$ = 55 °C) and adhesive resin ($T_{g,a}$ = 62 °C). The bond performance in the capacity and stiffness of the pullout response was substantially decreased when the temperature at the interface was over 70 °C.
- The strain distribution along the ETS-GFRP bar–concrete interface predicted by the developed bond model was slightly larger than those provided by the FEM simulation.
- One limitation of this study is the absence of experimental validation at elevated temperatures; therefore, future experimental investigations are required to further validate and calibrate the proposed thermo-mechanical bond–slip model. Future studies should also investigate the effects of key parameters such as embedment length, bar diameter, adhesive properties, and concrete strength to provide a more comprehensive understanding.

Acknowledgement

This study is funded by Murata Science and Education Foundation under grant number 25VH08.

References

[1] Khalifa A, Gold WJ, Nanni A, Abdel AMI (1998) Contribution of externally bonded FRP to shear capacity of RC flexural members. J Compos Constr 2(4):195-202. https://doi.org/10.1061/(ASCE)1090-0268(1998)2:4(195)

[2] Chaallal O, Mofidi A, Benmokrane B, Neale K (2011) Embedded through-section FRP rod method for shear strengthening of RC beams: performance and comparison with existing techniques. J Compos Constr 15(3):374-383. https://doi.org/10.1061/(ASCE)CC.1943-5614.0000174

[3] Bilotta A, Faella C, Martinelli E, Nigro E (2013) Design by testing procedure for intermediate debonding in EBR FRP strengthened RC beams. Eng Struct 46:147-154. https://doi.org/10.1016/j.engstruct.2012.06.031

[4] Le A.-T., Nguyen T.N., Cao V.V. (2023) Bond–slip behaviour of NSM GFRP bars in reinforced recycled-aggregate concrete: Experiments and a modified model. Civil Engineering Journal, 9(2):233. https://doi.org/10.28991/CEJ-2023-09-02-01

[5] Sengun K, Arslan G. Investigation of CFRP strengthening efficiency experimentally and analytically on reinforced concrete beams. Res. Eng. Struct. Mater., 2025; 11(5): 2351-2379. http://dx.doi.org/10.17515/resm2025-538me1119rs

[6] Sangeetha P, Prithvi R, Ashwin K V, Murali B, Yaashika M. Structural behavior of deficient hollow steel columns strengthened using GFRP. Res. Eng. Struct. Mater., 2025; 11(6): 2745-2760. http://dx.doi.org/10.17515/resm2025-541st1121rs

[7] Bourget S, El-Saikaly G, Chaallal O (2017) Behavior of reinforced concrete T-beams strengthened in shear using closed carbon fiber-reinforced polymer stirrups made of laminates and ropes. ACI Struct J 114(5). http://doi.org/10.14359/51700786

[8] Chalioris CE, Kosmidou PK, Papadopoulos NA (2018) Investigation of a new strengthening technique for RC deep beams using carbon FRP ropes as transverse reinforcements. Fibers 6(3). http://doi.org/10.3390/fib6030052

[9] Godat A, Chaallal O, Neale KW (2013) Nonlinear finite element models for the embedded through-section FRP shear-strengthening method. Comput Struct 119:12-22. https://doi.org/10.1016/j.compstruc.2012.12.016

[10] Breveglieri M, Aprile A, Barros JAO (2014) Shear strengthening of reinforced concrete beams strengthened using embedded through-section steel bars. Eng Struct 81:76-87. https://doi.org/10.1016/j.engstruct.2014.09.026

[11] Breveglieri M, Aprile A, Barros JAO (2015) Embedded through section shear strengthening technique using steel and CFRP bars in RC beams of different percentages of existing stirrups. Compos Struct 126:101-113. https://doi.org/10.1016/j.compstruct.2015.02.025
[12] Bui LVH, Stitmannaithum B, Ueda T (2020) Experimental investigation of concrete beams strengthened with embedded through-section steel and FRP bars. J Compos Constr 24(5):04020052. https://doi.org/10.1061/(ASCE)CC.1943-5614.0001055
[13] Bui LVH, Klippathum C, Prasertsri T, Jongvivatsakul P, Stitmannaithum B (2022) Experimental and analytical study on shear performance of embedded through-section GFRP-strengthened RC beams. J Compos Constr 26(5):04022046. https://doi.org/10.1061/(ASCE)CC.1943-5614.0001235
[14] Bui LVH, Stitmannaithum B (2020) Prediction of shear contribution for the FRP strengthening systems in RC beams: A simple bonding-based approach. J Adv Concr Technol 18:600-617. https://doi.org/10.3151/jact.18.600
[15] Bui LVH, Jongvivatsakul P, Stitmannaithum B, Likitlersuang S (2022) Numerical modelling of bond mechanism of ETS FRP bar–concrete joints with long embedment length. Int J Adhes Adhes 117:103179. https://doi.org/10.1016/j.ijadhadh.2022.103179
[16] Chen JF, Teng JG (2001) Anchorage strength models for FRP and steel plates bonded to concrete. J Struct Eng 127(7):784-791. https://doi.org/10.1061/(ASCE)0733-9445(2001)127:7(784)
[17] De Lorenzis L, Nanni A (2002) Bond between Near-Surface Mounted Fiber-Reinforced Polymer Rods and Concrete in Structural Strengthening. ACI Struct J 99(2). https://doi.org/10.14359/11534
[18] Dai JG, Sato Y, Ueda T (2005) Development of the nonlinear bond stress–slip model of fiber reinforced plastics sheet–concrete interfaces with a simple method. J Compos Constr 9(1):52-62. https://doi.org/10.1061/(ASCE)1090-0268(2005)9:1(52)
[19] Dai JG, Sato Y, Ueda T (2006) Unified analytical approaches for determining shear bond characteristics of FRP-concrete interfaces through pullout tests. J Adv Concr Technol 4(1):133-145. https://doi.org/10.3151/jact.4.133
[20] ACI (American Concrete Institute) (2017) Guide for the design and construction of externally bonded FRP systems for strengthening concrete structures. ACI PRC-440.2-17. Farmington Hills, MI: ACI
[21] JSCE (Japan Society of Civil Engineers) (2007) Recommendations for design and construction of concrete structures using continuous fiber reinforcing materials. Vol. C. Tokyo: JSCE
[22] CSA (Canadian Standards Association) (2012) Design and construction of building components with fiber-reinforced polymer. CAN/CSA S806-12. Rexdale, ON, Canada: CSA
[23] fib (Fédération Internationale du Béton) (2019) Externally applied FRP reinforcement for concrete structures. fib Bulletin 90. Lausanne, Switzerland: fib
[24] Gao WY, Teng JG, Dai JG (2012) Effect of temperature variation on the full-range behavior of FRP-to-concrete bonded joints. J Compos Constr 16(6):671-683. https://doi.org/10.1061/(ASCE)CC.1943-5614.0000296
[25] Dai JG, Gao WF, Teng JG (2013) Bond-Slip Model for FRP Laminates Externally Bonded to Concrete at Elevated Temperature. J Compos Constr 17:217-228. https://doi.org/10.1061/(ASCE)CC.1943-5614.0000337
[26] Godat A, L'Hady A, Chaallal O, Neale K (2012) Bond behavior of the ETS FRP bar shear-strengthening method. J Compos Constr 16:529-539. https://doi.org/10.1061/(ASCE)CC.1943-5614.0000280
[27] Caro M, Jemaa Y, Dirar S, Quinn A (2017) Bond performance of deep embedment FRP bars epoxy-bonded into concrete. Eng Struct 147:448-457. https://doi.org/10.1016/j.engstruct.2017.05.069
[28] Bui LVH, Stitmannaithum B, Ueda T (2020) Simulation of concrete beams strengthened by embedded through-section steel and GFRP bars with newly developed bond model. J Adv Concr Technol 18:364-385. https://doi.org/10.3151/jact.18.364
[29] Bui LVH, Klippathum C, Kongmalai N, Jongvivatsakul P, Ngo TD, Stitmannaithum B (2022) Analytical and numerical investigation of embedded through-section GFRP-strengthened RC beams with a developed bonding-based model. Eng Fract Mech 271:108595. https://doi.org/10.1016/j.engfracmech.2022.108595
[30] Abbasi A, Hogg PJ (2005) A model for predicting the properties of the constituents of a glass fibre rebar reinforced concrete beam at elevated temperatures simulating a fire test. Compos B Eng 36(5):384-393. https://doi.org/10.1016/j.compositesb.2005.01.005
[31] Shi JW, Cao WH, Wu ZS (2019) Effect of adhesive properties on the bond behaviour of externally bonded FRP-to-concrete joints. Compos B Eng 177:107365. https://doi.org/10.1016/j.compositesb.2019.107365
[32] He J, Xian G, Zhang YX (2021) Numerical modelling of bond behaviour between steel and CFRP laminates with a ductile adhesive. Int J Adhes Adhes 104:102753. https://doi.org/10.1016/j.ijadhadh.2020.102753
[33] ANSYS (2013) Finite element computer software for nonlinear structural analysis, version 15.0. Canonsburg, PA: Ansys Inc
[34] Hognestad E, Hanson NW, McHenry D (1955) Concrete stress distribution in ultimate strength design. ACI J Proc 52(12):455-479. https://doi.org/10.14359/11609